J Nanopart Res (2021) 23: 142
https://doi.org/10.1007/s11051-021-05257-7

RESEARCH PAPER

A facile approach for the preparation of NiONPs@MnO_2NRs nanocomposite material and its photocatalytic activity

Azeez O. Idris · Potlako J. Mafa · Ekemena O. Oseghe · Titus A. M. Msagati · Usisipho Feleni · Bhekie B. Mamba

Received: 26 June 2020 / Accepted: 3 June 2021 / Published online: 3 July 2021

Abstract Herein, a facile approach for preparing nickel oxide nanoparticles coupled with manganese oxide nanorods (NiONPs@MnO_2NRs) was reported for the first time. The nickel oxide nanoparticles, manganese oxide nanorods, and nanocomposite material were prepared using simple and inexpensive co-precipitation, hydrothermal, and sonication methods. The structural integrity of the composite materials was interrogated using field emission scanning electron microscopy (FESEM), energy-dispersive X-ray spectroscopy (EDS), transmission electron microscopy (TEM), X-ray diffraction (XRD), Fourier transform infrared (FTIR) spectroscopy, and ultraviolet–visible (UV–vis DRS) spectroscopy. FESEM and TEM results revealed an attachment of NiONPs onto the surface of MnO_2NRs. Electrochemical techniques, which included cyclic voltammetry (CV), linear sweep voltammetry (LSV), and electrochemical impedance spectroscopy (EIS), were employed to interrogate the electrochemical signature of the nanocomposite. The results revealed that these materials are potential nanomediator for the immobilisation of electroactive species in electrocatalysis and electrochemistry. Upon applying the materials in the photocatalytic degradation of 10 mg L^{-1} bromophenol blue dye, NiONPs@MnO_2NRs gave an efficiency of 81.5%, which was 2.8 and 4.3 folds higher than those obtained with NiONPs and MnO_2NRs materials, respectively. The electrochemical characterisation results confirmed an increased separation of electron–hole pairs, which helped enhance the photocatalytic activity of the composite material. The results further indicate that the prepared composite material can be explored with other organic water pollutants such as pesticides and pharmaceuticals.

Keywords Nickel oxide nanoparticles · Manganese (IV) oxide nanorods · Fluorine-doped tin oxide · Photocatalysis · Bromophenol blue

This article is part of the topical collection: Nanotechnology Convergence in Africa. Guest Editors: Mamadou Diallo, Abdessattar Abdelkefi, And Bhekie Mamba

Highlights
- Nickel nanoparticle was synthesised using cost-effective co-precipitation method.
- the hydrothermal synthetic route was used to prepare manganese nanorod.
- the simple facile approach was employed in preparing a hybrid of nanorods@nanoparticles.
- the NiONPs@MnO_2NRs nanocomposite can promote electron communication of conducting substrate

A. O. Idris (✉) · P. J. Mafa · E. O. Oseghe · T. A. M. Msagati · U. Feleni · B. B. Mamba
Institute for Nanotechnology and Water Sustainability (iNanoWS), College of Science, Engineering and Technology, University of South Africa, Florida Campus, Johannesburg 1709, South Africa
e-mail: idrisalone4real@gmail.com

Introduction

Over the years, scientists have been concerned about the high water contamination level and are therefore committed to getting rid of these contaminants (Rouse 2015). The synthesis of various analogues of nanomaterials and semiconductors has effectively tackled wastewater problems (Kuang et al. 2015). Several nanomaterials have been used as a photocatalyst in the oxidation of various organic pollutants. Among the nanomaterials, titanium dioxide (TiO_2) nanoparticles have played influential roles in decomposing various pollutants. However, this material exhibits a wider band gap (3.2 eV), making it difficult for the material to absorb light in the visible region. Also, since the solar spectrum comprises only 5% of the ultraviolet light, its photocatalytic potential cannot be appropriately harnessed (Dargahi et al. 2018). This has stimulated scientists in testing various visible-light active semiconductor photocatalysts for the oxidation of organic pollutants. Some of the most commonly applied visible-light active semiconductors include Cu_2O (Paula et al. 2019), Fe_2O_3 (Tang et al. 2018), Bi_2O_3 (Wang et al. 2019b), g-C_3N_4 (Kuang et al. 2015), MnO_2 (Ma et al. 2017), Ag_3VO_4 (Li et al. 2017), Ta_3N_5 (Wang et al. 2019a), and NiO (Muhambihai et al. 2020).

Nickel oxide (NiO) has attracted major attention due to its fascinating 3d electronic structure, that is localised in space but spread out over different energy range because of strong Coulomb repulsion between them (Liang et al. 2019). NiO is a p-type semiconductor with a wide bandgap (3.5 eV). The striking features of NiO include photosensitivity, low cost, abundant resources, huge light absorption, photoactive, stable under various pH, and ease of different morphological preparation (Liang et al. 2019). These qualities have stimulated their application in various fields such as batteries, supercapacitors, water splitting, and gas sensors (Liang et al. 2019). However, the pitfall of the application of NiO is due to the strong quantum confinement effects that increase the recombination of photogenerated electron–hole pair. Unfortunately, most semiconductors' major drawbacks in their application for photocatalysis are poor transport of charge carriers and fast recombination of photo-excited electron–hole pairs (Peleyeju and Arotiba 2018). These challenges are resolved by controlling the material's morphology, doping with noble metals, using catalysts, and constructing heterojunction using intelligent semiconductors (Peleyeju and Arotiba 2018). It is essential to highlight that the formation of heterojunction is the best method for resolving the drawbacks of the recombination of electron-holes (Peleyeju and Arotiba 2018). Moreover, the construction of p-type and n-type semiconductor heterojunction has been used to enhance the photocatalytic activity of semiconductors by elongating the charge carriers' lifespan through an efficient separation of the photogenerated electron–hole pair (Orimolade et al. 2019). Therefore, NiO has been coupled with various semiconductors such as $BiVO_4$ (Fu et al. 2019), SnO_2 (Alshehri et al. 2018), CdS (Chen et al. 2013), and WO_3 (Wu et al. 2018), among others to form the heterojunction that will discourage high rate of electron–hole pairs recombination.

In this work, manganese dioxide (MnO_2), a famous n-type semiconductor with a narrow bandgap of (2.33 eV), has been synthesised to construct heterojunction with NiO. The MnO_2 has been preferred as an excellent material of choice owing to its novel analytical features including high thermal stability, affordability, high surface area, environment-friendliness, catalytic properties, resource-rich biocompatible, and good compatibility with various analogues of carbon and other materials to form composites (Ma et al. 2017; Su et al. 2019). These qualities have attracted the use of MnO_2 in various fields such as biosensors (Mahajan et al. 2015; Wang et al. 2019d), lithium batteries (Kong et al. 2019; Liu et al. 2019), supercapacitors (Wang et al. 2019c; Zhang et al. 2019b), sensor (Dai et al. 2019; Wang et al. 2019c), and photocatalysis (Chen et al. 2016; Kumar et al. 2017). Different synthetic routes are used to prepare various morphologies of MnO_2 such as hydrothermal, co-precipitation, sol–gel, electrodeposition, and thermal decomposition (Zhao et al. 2016; Bai et al. 2018; Guan et al. 2018). Thus far, few reports on the application of MnO_2 for the degradation of organic pollutants have been documented in the literature. For instance, Humaira et al. employed MnO_2 and choline intercalated graphitic carbon nitride to mineralise 2,4-dichlorophenol and phenol. The nanocomposite material could

degrade 60 and 47% of the 2,4-dichlorophenol and phenol in 3600 s (Yasmeen et al. 2019). In another report, reduced graphene oxide was decorated on MnO_2 nanorods as adsorptive photocatalyst for the removal of coloured dye and ciprofloxacin in water (Chhabra et al. 2019). Quoling et al. constructed MnO_2/TiO_2 nano-tube arrays photoelectrodes for the completer removal of methylene orange (MO) in water (Ma et al. 2017). Similarly, the collaboration of TiO_2 and MnO_2 nanostructure was used in the degradation of toluene. The heterostructure assisted in suppressing the recombination of photogenerated electron–hole pairs (Zhang et al. 2019a). Furthermore, various heterostructures of MnO_2 such as MnO_2/TiO_2 (Ma et al. 2017), $BiVO_4/MnO_2$ (Trzci et al. 2016), and MnO_2/WO_3 (Ouyang et al. 2019) have been reported to display better-quality catalytic activities towards the decomposition of various organic pollutants under light irradiation.

In this study, we report on a simple method for synthesising nickel oxide nanoparticles@manganese (IV) oxide nanorods (NiONPs@MnO_2NRs), and it was interrogated for photocatalytic degradation of bromophenol blue dye for the first time based on our knowledge. Our environment is facing unprecedented challenges of pollution from different organic pollutants such as dyes, and it is imperative to find ways to mitigate the impact of this problem. Hence, this study adds to the knowledge of photocatalysis that has been established, and the composite material is employed in such studies for the first time.

Materials and methods

Chemicals and sample preparation

Potassium permanganate ($KMnO_4$), manganese sulphate monohydrate ($MnSO_4•H_2O$), sodium hydroxide (NaOH), potassium hexacyanoferrate (II) [$K_4Fe(CN)_6$], nickel nitrate hexahydrate $(NiNO_3)_2•6H_2O$, sodium sulphate (Na_2SO_4), potassium chloride (KCl), isopropanol (C_3H_8O), ethanol (C_2H_5OH), potassium hexacyanoferrate (III) [$K_3Fe(CN)_6$], and bromophenol blue ($C_{19}H_{10}Br_4O_5S$). The reagents were purchased from Sigma-Aldrich, Germany.

Synthesis of NiONPs

NiONPs were synthesised by a simple and cost-effective co-precipitation method. Briefly, a mixture of 2 M $(NiNO_3)_2•6H_2O$ and 1 M aqueous KOH solution was stirred for 3 h at ambient temperature, and the resulting precipitate was washed with distilled water to remove K^+ and dried in the oven at 70 °C. The dried sample was grounded and calcinated at 750 °C for 150 min. The proposed equations for the synthesis are presented in Eqs. 1 and 2:

$$Ni\left(NO_3\right)_{2(s)} + KOH_{(s)} \rightarrow Ni(OH)_{2(s)} + KNO_{3(aq)} \quad (1)$$

$$Ni(OH)_{2(s)} \rightarrow NiO_{(s)} + H_2O_{(l)} \quad (2)$$

Preparation of MnO_2 nanorod

The MnO_2 nanorod was synthesised by adding a mixture of 0.5 g manganese sulphate (VI) monohydrate and 1.26 g of potassium permanganate to 35 mL deionised water. The resulting mixture was transferred into a Teflon-lined autoclave and heated at 180 °C for half a day. The precipitate formed was washed copiously with a mixture of ethanol and water, and the final product was oven-dried at 80 °C to form a dark brown manganese nanorod (Idris and Arotiba 2018). The proposed equation for the synthesis is presented in Eq. 3:

$$3MnSO_{4(s)} + 2KMnO_{4(s)} + 2H_2O_{(l)} \rightarrow K_2SO_{4(aq)} + 2H_2SO_{4(aq)} + 5MnO_{2(s)} \quad (3)$$

Synthesis of NiONPs@MnO_2NRs heterostructure

Equal masses of MnO_2 and NiONPs were separately dispersed in 30 mL ethanol by ultrasonication for half an hour. The two suspensions were mixed and ultrasonicated for 30 min. Subsequently, the mixture was vigorously stirred for 180 min, dried in an oven overnight at 60 °C.

Characterisation

The FESEM images were obtained on a JEOL JSM-7800F field emission scanning electron microscope (FESEM) coupled with Thermo Scientific Ultradry EDS detector (Thermo Fisher Scientific,

Waltham, MA, USA). The TEM and SAED results were recorded using a Tecnai G^2F_2O X-Twin MAT (FEI Company, Eindhoven, Netherlands) operating at 200 kV. Rigaku SmartLab X-ray diffractometer (Rigaku Corporation, Tokyo, Japan) with CuKα ($\lambda = 0.154059$ nm) radiation was used for XRD analysis. PerkinElmer FTIR spectrometer Frontier™ (spectrum 100 spectrometer) was employed for functional group analysis using the KBr pellet method. Thermogravimetric analysis (TGA) of the materials was done under nitrogen at a flow rate of 50 mL min^{-1}. It was heated from ambient temperature to 1000 °C at a heating rate 10 °C min^{-1}, using a thermogravimetric TGA 5500. The UV–vis DRS spectra were recorded using PerkinElmer Lambda™ 6505 UV–vis spectrometer from 200 to 800 nm, and $BaSO_4$ was used as the reference material.

Preparation of NiONPs, MnO_2NRs, and NiONPs@MnO_2NRs electrodes

The electrodes were prepared by adding 1 mg of NiONPs, MnO_2NRs, and NiONPs@MnO_2NRs into the mixture (20 µL Nafion and 20 µL of isopropanol). Consequently, the mixture was sonicated for 1 h and drop coated onto the FTO surface (50 mm × 13 mm × 3 mm) with surface resistivity of − 8 Ω/sq. These modified electrodes were placed in the oven at 35 °C for few hours. The resulting products were meticulously rinsed with deionised water and labelled as FTO/NiONPs, FTO/MnO_2NRs, and FTO/NiONPs@MnO_2NRs electrodes. Finally, electrochemical characterisation was done on a potentiostat/galvanostat (Autolab, PGSTAT 302 N model, Metrohm, Swiss instruments), using a three-electrode configuration. The working, counter, and reference electrodes were FTO, platinum wire, and Ag/AgCl (3 M KCl), respectively. The electrochemical studies, including charge transfer features of the fabricated electrodes, were investigated using 5 mM $[Fe(CN)_6]^{3-/4-}$ probe prepared in 0.1 M KCl solution using CV, LSV, and EIS.

Photocatalytic performance

The photocatalytic performance of the materials was evaluated using bromophenol (BPB) (50 mL of 10 mg L^{-1}) blue dye as a model organic pollutant. The experiment started with an establishment of adsorption–desorption equilibrium in which 30 mg of catalyst was stirred in 50 mL of BPB solution for 30 min. The simulated light from ASAHI HAL-320 solar simulator with irradiation of 300 W from Xenon lamp was used for the photodegradation experiment while continuously stirring the suspension. At a pre-determined time interval, the 3 mL aliquots were samples and analysed with Lambda 6505 PerkinElmer UV–vis spectrometer after filtered through 0.45-µm GHP Acrodisc 13 (Pall) filters (Pall Corporation, Port Washington, NY, USA). The removal efficiency (RE (%)) was calculated as follows:

$$RE(\%) = \left(1 - \frac{C_t}{C_0}\right) \times 100\% \quad (4)$$

Results and discussion

FESEM and EDX analysis

The FESEM images of the semiconductors were taken to confirm their morphologies. As seen in (Fig. 1a), the MnO_2NRs exhibited a rod-shaped morphology while the NiONPs obtained spherically shaped particles (Fig. 1b). In contrast, the nanocomposite of NiONPs@MnO_2NRs exhibited the synergy of both rod and spherical shape-like morphologies as illustrated in (Fig. 1c). This observation was further confirmed by EDX analysis (Fig. 1d), which revealed nickel, manganese, and oxygen in the NiONPs@MnO_2NRs nanocomposite material.

TEM analysis

The morphology of the prepared nanomaterials was investigated using TEM. Figure 2 presents the images of the nanomaterials and their corresponding selected area electron diffraction (SAED) patterns. The MnO_2NRs revealed a rod shape-like morphology with the diameter range of 17.3–35.4 nm (Fig. 2a). On the HRTEM image of MnO_2, fringes were observed with inter-planar distance of 0.316 nm indexed to (310) crystal plane of MnO_2. This agrees with XRD results. The bulk defects were also observed on HRTEM image of MnO_2. It is reported that bulk defects immerge due to lack of oxygen in the materials (Zhu et al. 2017). On the other hand, the TEM

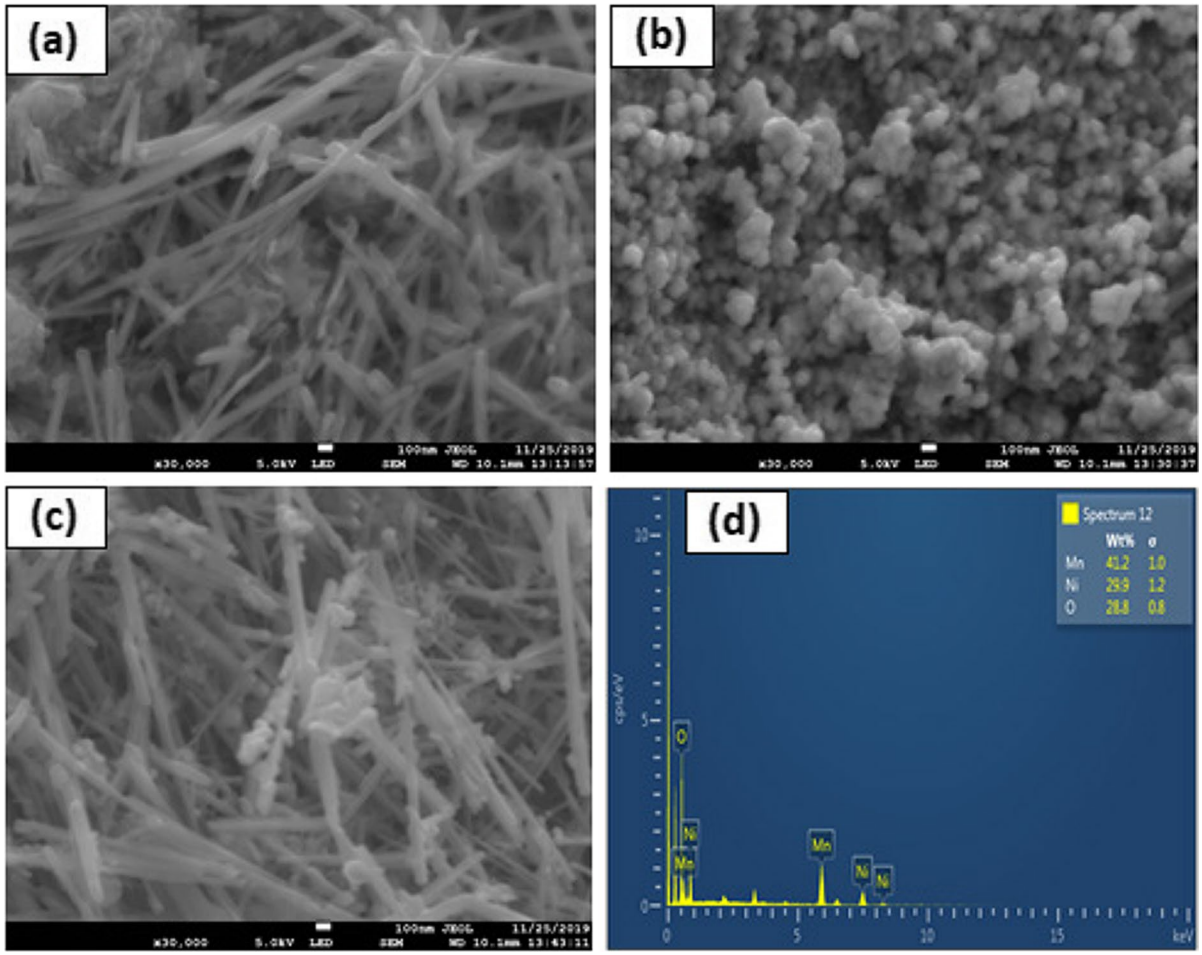

Fig. 1 FESEM images of **a** MnO_2NRs, **b** NiONPs, and **c** NiONPs@MnO_2NRs at 100 nm scale view. **d** EDS spectrum of NiONPs@MnO_2NRs

images of NiONPs were displaying the sphere and cubic-like morphologies. The diameters of the particles were determined to be 19.5 nm for sphere and 25.4–33.7 nm for cubic ones (Fig. 2b). The nanocomposite of NiONPs@MnO_2NRs revealed a hybrid of rod and spherical shape morphology (Fig. 2c) and the morphology proved that the two photocatalysts were blended together to form a composite catalyst that could be ideal for photocatalytic applications. The inter-planar distance of 0.341 nm corresponding to (310) plane of MnO_2 was observed while there were no fringes observed got NiONPs. The interfacial contact of MnO_2NRs and NiONPs could be a reason for effective catalytic degradation of BPB pollutant. The TEM-SAED analysis was used as another method for an in-depth understanding of the crystallinity of the materials. The well-defined ring formation in the SAED patterns illustrates the materials' high-crystallinity nature as shown in Fig. 2a–c.

XRD analysis

The crystallinity of the as-prepared materials was assessed by X-ray diffraction analysis, as shown in Fig. 3. The peaks observed in NiONPs diffractogram located at 37.3°, 43.4°, 63.0°, 75.5°, and 79.5° could be indexed to (111), (200), (220), (311), and (222) of the cubic phase structure of NiO as per the standard spectrum card (JCPDS No.: 04–0835) (Sankar et al. 2016). For pure MnO_2NRs, the peaks centred at 17.0°, 24.1°, 28.8°, 37.7°, 49.9°, and 60.1° were ascribed to (200), (220), (310), (221), (411), and

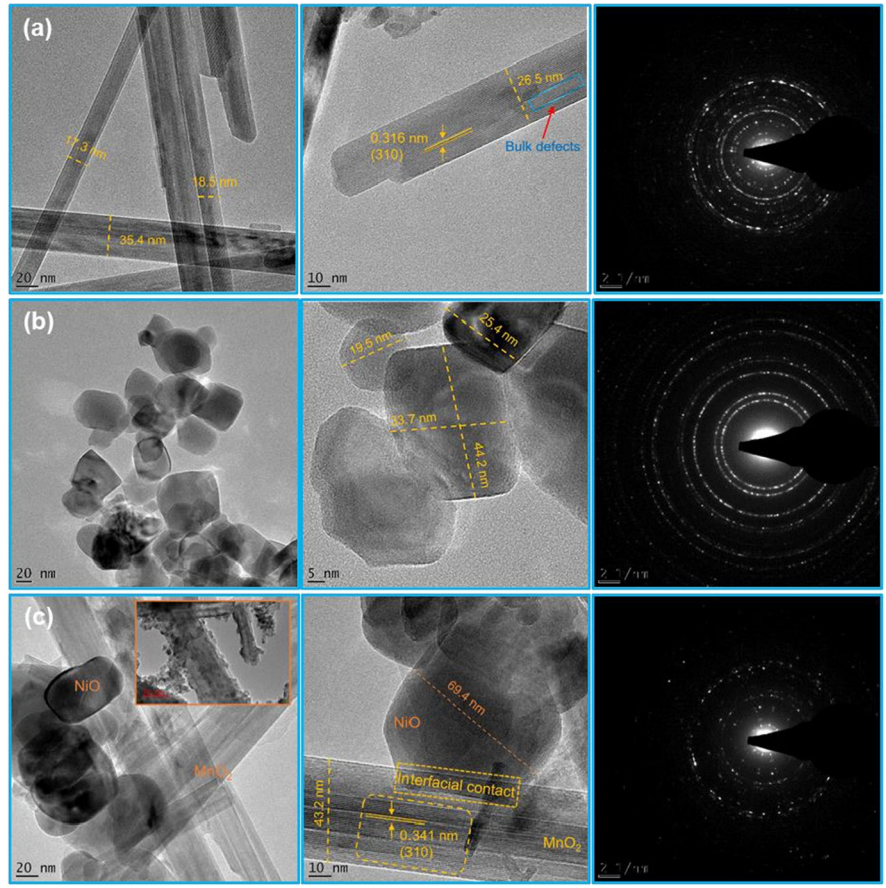

Fig. 2 TEM/HRTEM images and corresponding SAED pattern of **a** MnO_2NRs, **b** NiONPs, and **c** NiONPs@MnO_2NRs photocatalysts

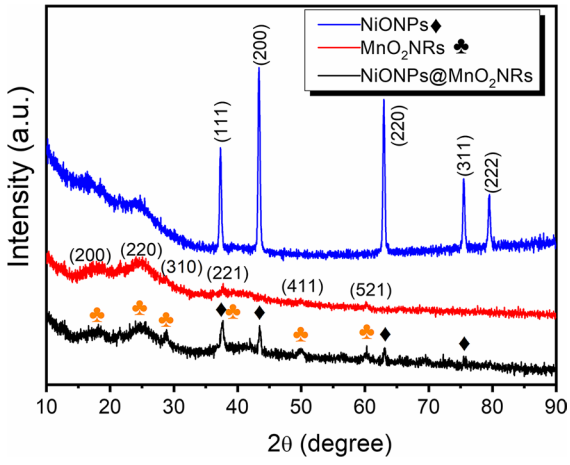

Fig. 3 XRD diffractograms of the three synthesised catalysts

(521) of α-MnO_2 according to JCPDS No.: 44–0141 (Guo et al. 2020). Furthermore, the peaks corresponding to both NiONPs and MnO_2NRs were observed in the XRD pattern of the composite material, confirming the co-existence of the two pristine materials in the composite prepared. The interfacial contact developed here would be beneficial for the performance of the composite for photodegradation purposes. The crystallite sizes (D) were also determined using Debye–Scherrer equation (Sithole et al. 2021):

$$D = \frac{0.9\lambda}{\beta Cos\theta} \tag{5}$$

where λ is the CuKα radiation wavelength (0.15418 nm), β is the full width at half maximum (FWHM) in radians, and θ is the Bragg angle. The values of D were determined to be 13.9, 32.6, and 16.2 nm for MnO_2, NiO, and NiO@MnO_2,

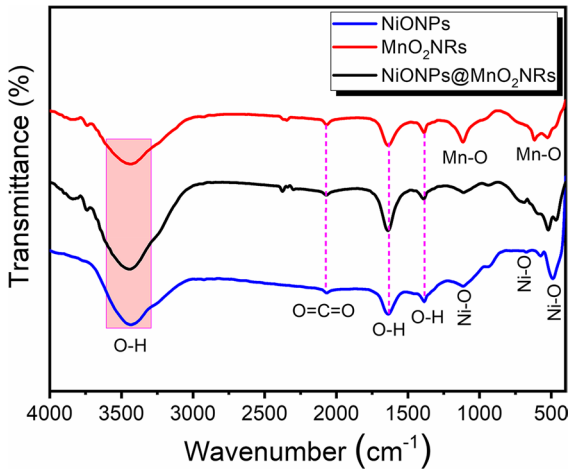

Fig. 4 FTIR spectra of the nanomaterials

respectively. The crystallite sizes for these catalysts are very close to particle sizes determined by TEM results.

FTIR analysis

The functional groups present in the nanomaterials were interrogated using FTIR (Fig. 4). The peak around 492 and 679 cm^{-1} is due to the Ni–O bond stretching vibrations. The broadness of the peak revealed that the NiONPs are crystalline. The absorption band at 2078 cm^{-1} is because of the symmetric and the asymmetric stretching mode of vibrations of the carbon dioxide molecule absorbed from the air (Jayakumar et al. 2017). More so, the broad peak at 3431, 1387, and 1638 cm^{-1} can be accredited to the stretching and bending vibration of –OH group absorbed on the nanomaterial surface (Jayakumar et al. 2017). For the MnO_2NRs, the broadband at 3430 cm^{-1} is attributed to the stretching vibrations of hydrogen-bonded surface water molecules and hydroxyl groups. In comparison, the bands at 1637 and 1384 cm^{-1} represent quantum numbers of residual –OH groups, which involve the O–H vibration mode of traces of adsorbed water. The band at 519 cm^{-1} can be attributed to the Mn–O vibrations of MnO_2 nanorod (Pradeep Kumar et al. 2014). Finally, the bands at 531 and 695 cm^{-1} revealed that Ni–O stretching vibration of NiONPs and Mn–O vibration of MnO_2NRs are present in the nanocomposite. The presence of more O–H groups on the surface of catalysts could help in production of more hydroxyl radicals.

Thermal analysis

Thermogravimetric analysis is essential in showing the thermal stability of any material. Figure 5 shows the TGA curves for the different materials and revealed that they are relatively stable. However, MnO_2NR is the most stable (weight loss ≈ 3%) material, while NiONPs@MnO_2NRs is the least stable material (weight loss ≈ 11%). It has been reported that weight loss under 250 °C as seen in this study is due to the evaporation of surface adsorbed and interlayer water (Liu et al. 2016). Further weight loss after 500 °C could be due to the successive dehydroxylation to form a metal oxide, as reported by Bandar et al. (2021). The unique TGA curve for NiONPs@MnO_2NRs is an indication that the composite material with properties different from NiONPs and MnO_2NRs is formed.

Optical analysis

The optical properties of the synthesised NiONPs, MnO_2NRs, and NiONPs@MnO_2NRs were examined using UV–visible reflectance spectroscopy, as shown in Fig. 6a. The absorption edges are attributed to 325 nm, 628 nm, and 642 nm for NiONPs, MnO_2NRs, and NiONPs@MnO_2NRs. The Tauc formula (Eq. 6) was employed in calculating the band energy of the semiconductor, as depicted in Fig. 6b.

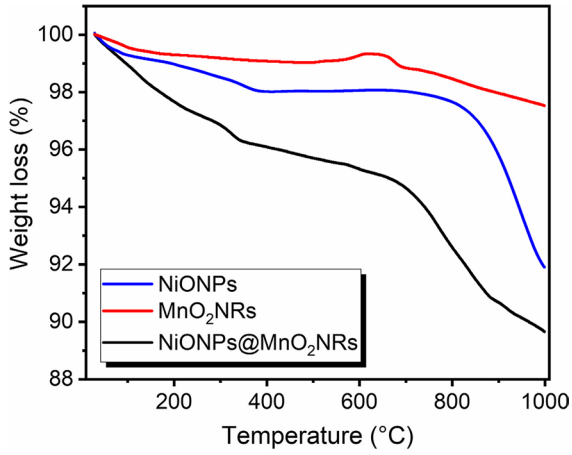

Fig. 5 Thermograms of the prepared materials

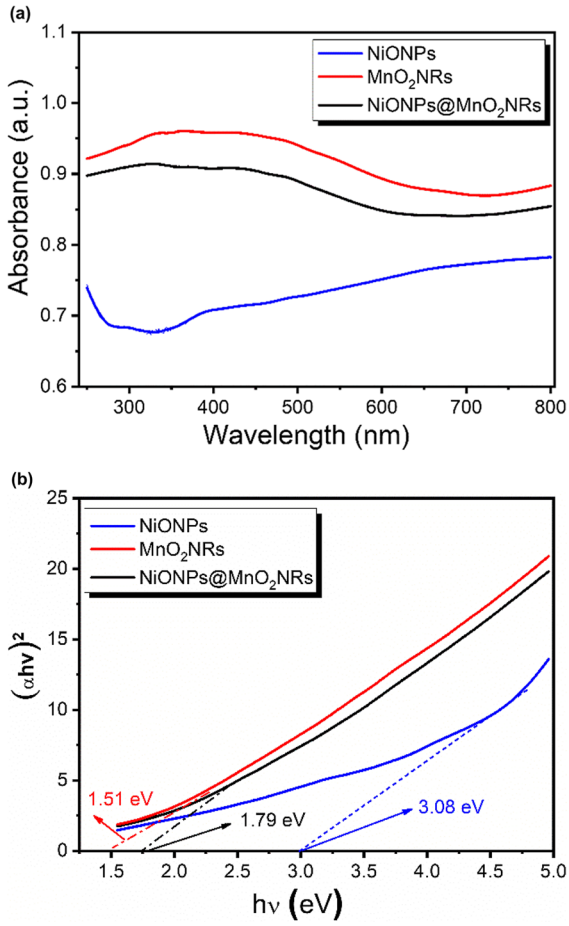

Fig. 6 **a** UV–visible diffuse reflectance spectra and **b** bandgap edges of the semiconductors

$$\alpha h\nu = A\left(h\nu - E_g\right)^{n/2} \tag{6}$$

where α, h, A, E_g, and ν are the absorption coefficient, Planck's constant, constant, bandgap incident light frequency and n is constant, which relies mainly on the optical transition features of the materials such as MnO_2, the value of n is 1 (Umukoro et al. 2018). The plot of $(\alpha h\nu)^2$ versus hν was plotted, and the E_g values of the semiconductors were 3.08 eV, 1.51 eV, and 1.79 eV, respectively. This reduction in the energy bandgap can be ascribed to the heterojunction form between the p-NiONPs and the n-MnO_2NRs. The narrow bandgap energy obtained from the nanocomposite revealed that it absorbs light at the visible region and can play pivotal roles for various environmental and photocatalytic applications.

Electrochemical characterisation of the nanomaterials

The FTO/NiONPs, FTO/MnO_2NRs, and FTO/NiONPs@MnO_2NRs electrodes were characterised using CV, LSV, and EIS in 5 mM $[Fe(CN)_6]^{3-/4-}$ redox probe prepared in 0.1 M KCl as supporting electrolyte. The CV results (Fig. 7a) revealed that FTO/NiONPs@MnO_2NRs electrode gave the highest faradaic current signal, followed by FTO/NiONPs and FTO/MnO_2NRs. More so, the electroactive surface area was calculated using Randles–Sevcik equation (Eq. 7):

$$I_p = \left(2.69 \times 10^5\right) n^{3/2} AC(D\upsilon)^{1/2} \tag{7}$$

where I_p = peak current, n = number of electrons exchanged in the reaction, A = area of electrode active surface (cm^2), C = concentration (mol cm^{-3}), D = diffusion coefficient of ferrocyanide is 7.6×10^{-6} (cm^2 s^{-1}), and υ = scan rate (V s^{-1}). The electroactive surface areas of the electrode at a scan rate of 50 mV s^{-1} were 0.863, 0.809 cm^2, and 0.202 cm^2 for FTO/NiONPs@MnO_2NRs, FTO/NiONPs, and FTO/MnO_2NRs, respectively. The highest electroactive surface area was obtained from the electrode fabricated from the nanocomposite. In addition to this, the LSV was done in the same redox probe as the CV experiment. The current vs. potential plot is shown in Fig. 7b using a potential range from − 0.2–0.5 V and a scan rate of 50 mV s^{-1}. The linear voltammograms revealed that peak currents of 0.00376 A, 0.00284 A, and 0.000678 A were obtained for FTO/NiONPs@MnO_2NRs, FTO/NiONPs, and FTO/MnO_2NRs, respectively. The NiONPs@MnO_2NRs gave the highest peak current response, which agrees with the CV result. The improvement in the peak current response is ascribed to the synergistic effect of the NiONPs and MnO_2NRs.

Furthermore, the electrochemical impedance spectroscopy technique was used to interrogate the prepared electrodes' charge-transfer properties using a bias potential of + 0.5 V. The Nyquist plots for the fabricated electrodes (Fig. 7c) were used to predict the electrodes' charge transfer resistance (Rct). The semi-circular arc (Fig. 7c) gave crucial evidence on

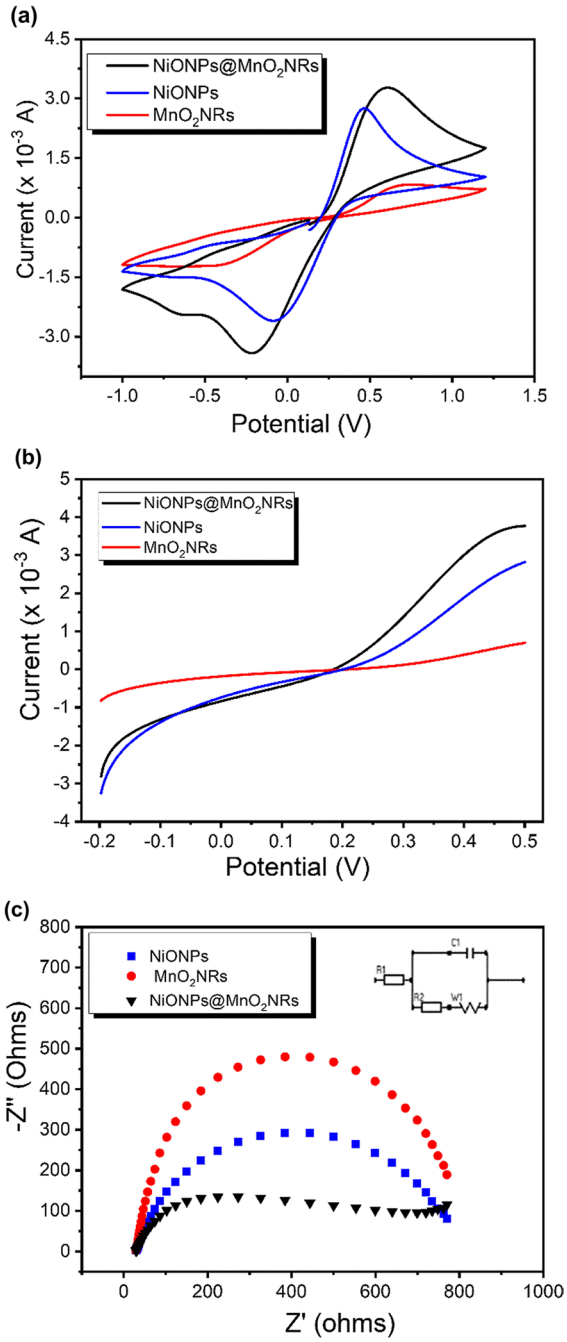

Fig. 7 **a** Cyclic voltammetry, **b** linear sweep voltammetry, and **c** EIS of FTO/MnO_2NRs, FTO/NiONPs, and FTO/NiONPs@MnO_2NRs electrodes

the R_{ct} of the semiconductors. It is essential to highlight that the lower the arc radius, the greater the charge transfer efficiency and better electron transfer

Table 1 Electrical information obtained from the Randles equivalent circuit fitting inset in Fig. 7c

Circuit element	FTO-NiONPs	FTO/MnO_2NRs	FTO/NiONPs@MnO_2NRs
R_s (Ω)	29.73	28.74	28.51
R_{ct} (Ω)	861.76	1395.80	472.36
CPE (nF)	26.30	15.56	12.62

performance. A fast and efficient charge transfer at the electrode–electrolyte interface can hinder the recombination of charges, which results in the improvement in the effective separation of photogenerated electrons and holes. Thus, NiONPs@MnO_2NRs gave the highest charge transfer efficiency followed by NiONPs and MnO_2NRs, respectively, as depicted in Table 1. The EIS results corroborated the results obtained from CV and LSV, respectively. Besides, the electron transfer apparent rate constant (k_{app}) associated with the charge was determined using Eq. 8 (Ntsendwana et al. 2013):

$$k_{app} = \frac{RT}{F^2 R_{ct} C} \tag{8}$$

R is the ideal gas constant, T is the absolute temperature, C is the concentration of $[Fe(CN)_6]^{3-/4-}$, and R_{ct} is the charge transfer resistance. The K_{app} values of 11.3×10^{-5}, 6.18×10^{-5}, and 3.81×10^{-5} cm s^{-1} were obtained for FTO/NiONPs@MnO_2NRs, FTO/NiONPs, and FTO/MnO_2NRs, respectively. These K_{app} results further confirmed that the high electrochemical kinetics were in FTO/NiONPs@MnO_2NRs, followed by FTO/NiONPs, and lastly, FTO/MnO_2NRs. The results agree well with CV, LSV, and EIS Nyquist results.

Photocatalytic performance

The photocatalytic performance of the materials was evaluated using bromophenol (BPB) (50 mL of 10 mg L^{-1}) blue dye as a model organic pollutant. The experiment started with an establishment of adsorption–desorption equilibrium for 30 min in the dark. After that, the simulated solar light was illuminated onto the suspension. Figure 8a displays UV–vis spectra of BPB at 591 nm (wavelength of maximum absorption) as a function of reaction time. It was

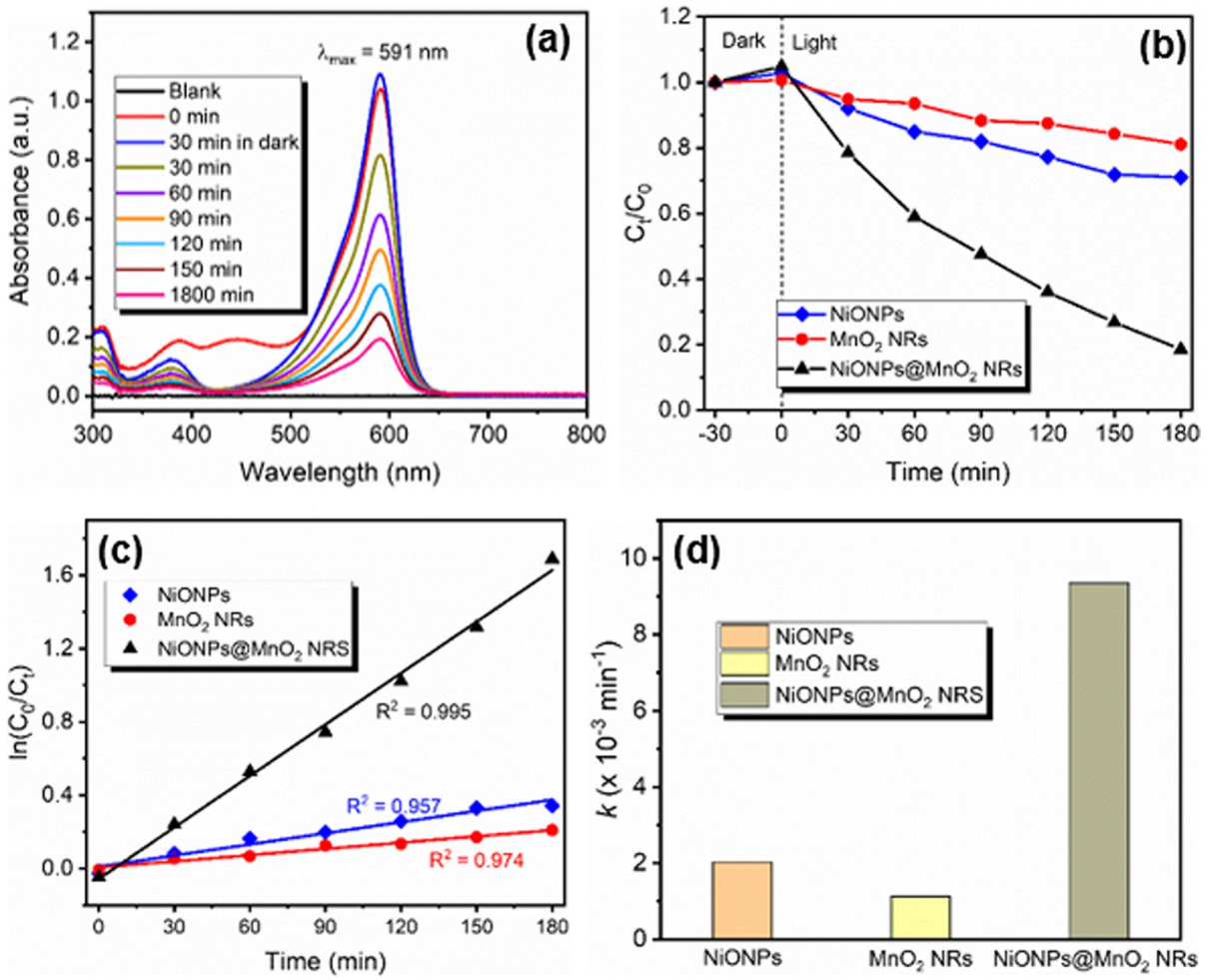

Fig. 8 **a** UV–vis absorbance spectra of BPB dye versus time, **b** ratio of concentrations as a function of time, **c** pseudo-first-order kinetics of different catalysts, and **d** bar chart of rate constants for different catalysts

decreasing with an increase in irradiation time to 180 min. This showed that the chromophore responsible for 591 nm was indeed getting reduced in the presence of NiONPs@MnO_2NRs catalyst. As shown in Fig. 8b, all the catalysts were tested for the degradation of BPB under simulated light. The removal efficiencies of 18.9, 29.0, and 81.5% were obtained in the presence of MnO_2NRs, NiONPs, and NiONPs@MnO_2NRs composite catalysts, respectively. The enhanced photocatalytic performance displayed by the NiONPs@MnO_2NRs composite catalyst is attributed to the ability of the catalyst to harvest visible light to due to its narrow band gap energy, synergistic interaction between the interface of the two materials, high oxidation and reduction power of the catalyst as shown in the CV, high electron transfer mobility shown in the LSV, and high charge transfer efficiency and low resistance as illustrated by Nyquist plots (Mafa et al. 2020b). The composite catalyst showed high electron–hole separation, which contributed to the degradation of BPB dye.

The photocatalytic degradation of BPB dye on MnO_2NRs, NiONPs, and NiONPs@MnO_2NRs composite catalysts was fitted with a Langmuir–Hinshelwood first-order model displayed by Eq. 9 (Mafa et al. 2020a) (Fig. 8c):

$$ln\left(\frac{C_0}{C_t}\right) = k_{app}t \tag{9}$$

where the slope of $\ln(C_0/C_t)$ versus time (t) gives the apparent rate constant (k_{app}). The obtained apparent rate constants for MnO_2NRs, NiONPs, and NiONPs@MnO_2NRs composite catalysts were 0.00113, 0.00202, and 0.00935 min^{-1} as indicated by a bar chart in Fig. 8d. Malefane reported that the beneficial effect of pristine catalysts in the composite could be evaluated by synergy factor (SF) deduced from the calculated apparent rate constants as given by Eq. 10 (Malefane 2020):

$$SF = \frac{K_{NiONPs@MnO2NRs}}{K_{NiONPs} + K_{MnO2NRs}} \quad (10)$$

The synergy factor (SF) for NiONPs@MnO_2NRs composite catalyst was 2.97 for BPB dye degradation. This confirmed that the synergistic interaction between the pristine materials was feasible and occurred to improve photocatalytic activity.

Photocatalytic performance

In photocatalytic degradation of organic pollutants, reactive oxygen species such as superoxide ($^{\cdot}O_2^-$) and hydroxyl ($^{\cdot}OH$) are remarkably responsible for the destruction of organics on the surface of semiconductor materials (Mafa et al. 2021). As shown in Fig. 9, the degradation of BPB dye on the surface of NiONPs@MnO_2NRs catalyst was proposed as depicted. NiONPs are p-type, while the MnO_2NRs are n-type semiconductors. In p-n heterojunction formed, both NiONPs and MnO_2NRs absorb light of energy equal or bigger than their band gaps. The electrons are excited from valence bands (VBs) of both materials to their conduction bands (CBs), leaving holes behind. The photogenerated electrons would migrate from the CB of p-NiONPs to the CB of n-MnO_2NRs due to the CB offset. Likewise, the holes in the VB of MnO_2NRs would migrate to the VB of NiONPs driven by offset difference. The photogenerated electrons and holes are stabilised by the redistribution of electrons on the CB of n-MnO_2NRs and holes on the VB of p-NiONPs, respectively (Nikokavoura and Trapalis 2018). This phenomenon inhibits the recombination of photogenerated electrons and holes and promotes their long lifetime, and significantly improved photocatalytic process. The electrons on the CB of n-MnO_2NRs participate in reducing reactions with molecular oxygen to produce superoxide radicals. The holes in the VB of p-NiONPs partake in the oxidation of hydroxyl ions into hydroxyl radicals and in direct degradation of BPB pollutants. The reactive oxygen radicals generated participated in photocatalytic degradation of BPB dye, as shown in Fig. 9. The p-n heterojunction formed is very vital for longer separation of electron–hole pairs.

Conclusion

This work demonstrates the synthesis of nickel oxide nanoparticles, manganese oxide nanorods, and composite material. The composite materials' structural integrity was interrogated using thermal,

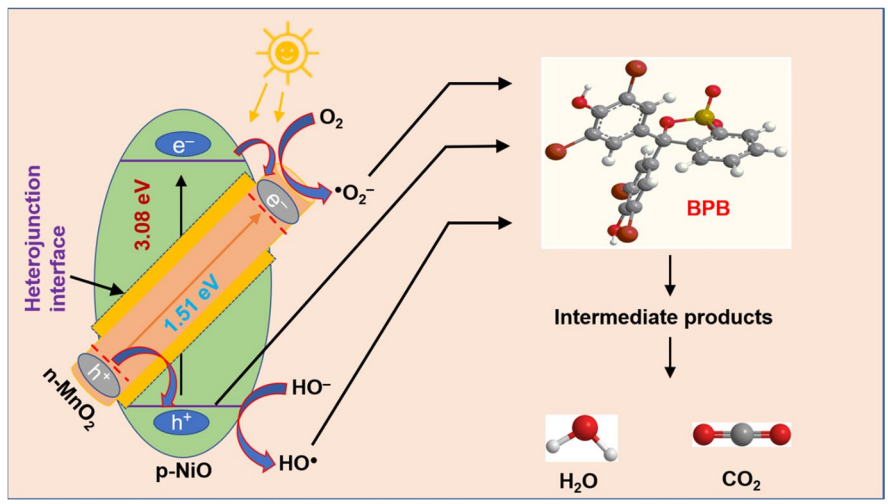

Fig. 9 Proposed electron–hole separation and degradation mechanism of BPB on NiONPs@MnO_2NRs catalyst

crystallographic, different microscopic, and spectroscopic techniques. These techniques revealed the successful preparation of the pristine and nanocomposite material. The FESEM and TEM results showed the formation of NiONPs on the surface of MnO_2NRs with nano-ranged sizes. The electrochemical analysis displayed that the NiONPs@MnO_2NRs had improved electrochemical activities than the pristine materials and reduced the electron–hole recombination rate. This was associated with the high removal efficiency of 81.5% obtained with composite catalysts over 18.9 and 29.0% obtained with MnO_2NRs and NiONPs. The NiONPs@MnO2NRs material's applicability clearly shows that this material can be explored further for various organic pollutants degradation, electrochemical energy production, and drug delivery research.

Acknowledgements The authors acknowledge the Institute for Nanotechnology and Water Sustainability (iNanoWS), University of South Africa.

Compliance with ethical standards

Conflict of interest The authors declare no competing interests.

References

Alshehri M, Al-marzouki F, Alshehrie A, Hafez M (2018) Synthesis, characterization and band alignment characteristics of NiO/SnO_2 bulk heterojunction nanoarchitecture for promising photocatalysis applications. J Alloys Compd 757:161–168

Bai X, Tong X, Gao Y et al (2018) Hierarchical multidimensional MnO_2 via hydrothermal synthesis for high performance supercapacitors. Electrochim Acta 281:525–533. https://doi.org/10.1016/j.electacta.2018.06.003

Bandar S, Anbia M, Salehi S (2021) Comparison of MnO_2 modified and unmodified magnetic Fe_3O_4 nanoparticle adsorbents and their potential to remove iron and manganese from aqueous media. J Alloys Compd 851:156822. https://doi.org/10.1016/j.jallcom.2020.156822

Chen X, Chen W, Lin P et al (2013) In situ photodeposition of nickel oxides on CdS for highly efficient hydrogen production via visible-light-driven photocatalysis. Catal Commun 36:104–108

Chen H, Liu XY, Hao XD, Xin Y (2016) Facile biphasic synthesis of TiO_2–MnO_2 nanocomposites for photocatalysis. Ceram Int 42:19425–19428. https://doi.org/10.1016/j.ceramint.2016.08.160

Chhabra T, Kumar A, Bahuguna A, Krishnan V (2019) Reduced graphene oxide supported MnO_2 nanorods as recyclable and efficient adsorptive photocatalysts for pollutants removal. Vacuum 160:333–346

Dai Y, Huang J, Zhang H, Chiun C (2019) Highly sensitive electrochemical analysis of tunnel structured MnO_2 nanoparticle-based sensors on the oxidation of nitrite. Sensors Actuators B Chem 281:746–750. https://doi.org/10.1016/j.snb.2018.11.014

Dargahi Z, Asgharzadeh H, Maleki-ghaleh H (2018) Synthesis of Mo-doped TiO_2/reduced graphene oxide nanocomposite for photoelectrocatalytic applications. Ceram Int 44:13015–13023. https://doi.org/10.1016/j.ceramint.2018.04.120

Fu Y, Zhao J, Wang H et al (2019) All-solid-state Z-scheme system of NiO/CDs/$BiVO_4$ for visible light-driven efficient overall water splitting. Chem Eng J 358:134–142. https://doi.org/10.1016/j.cej.2018.10.005

Guan S, Li W, Ma J et al (2018) A review of the preparation and applications of MnO_2 composites in formaldehyde oxidation. J Ind Eng Chem 66:126–140. https://doi.org/10.1016/j.jiec.2018.05.023

Guo R, Wang Y, Li J et al (2020) Sulfamethoxazole degradation by visible light assisted peroxymonosulfate process based on nanohybrid manganese dioxide incorporating ferric oxide. Appl Catal B Environ 278:119297. https://doi.org/10.1016/j.apcatb.2020.119297

Idris AO, Arotiba OA (2018) Towards cancer diagnostics – an a-feto protein electrochemical immunosensor on a manganese (IV) oxide/gold nanocomposite immobilisation layer. RSC Adv 8:30683–30691. https://doi.org/10.1039/C8RA06135A

Jayakumar G, Irudayaraj AA, Raj AD (2017) Photocatalytic degradation of methylene blue by nickel oxide nanoparticles. Mater Today Proc 4:11690–11695. https://doi.org/10.1016/j.matpr.2017.09.083

Kong S, Gong Y, Liu P et al (2019) Synthesis of lithium rich layered oxides with controllable structures through a MnO_2 template strategy as advanced cathode materials for lithium ion batteries. Ceram Int 45:13011–13018. https://doi.org/10.1016/j.ceramint.2019.03.231

Kuang P, Su Y, Chen G et al (2015) g-C3N4 decorated ZnO nanorod arrays for enhanced photoelectrocatalytic performance. Appl Surf Sci 358:296–303. https://doi.org/10.1016/j.apsusc.2015.08.066

Kumar V, Fakhri A, Agarwal S et al (2017) Synthesis and characterization of MnO_2/NiO nanocomposites for photocatalysis of tetracycline antibiotic and modification with guanidine for carriers of caffeic acid phenethyl ester-an anticancer drug. J Photochem Photobiol B Biol 174:235–242. https://doi.org/10.1016/j.jphotobiol.2017.08.006

Li S, Hu S, Jiang W et al (2017) Facile synthesis of flower-like Ag_3VO_4/Bi_2WO_6 heterojunction with enhanced visible-light photocatalytic activity. J Colloid Interface Sci 501:156–163. https://doi.org/10.1016/j.jcis.2017.04.057

Liang Z, Huang R, Liang R et al (2019) Preparation of a shell nanostructure for highly selective photocatalytic oxidation of organic compounds by wrapping on NiO nanorods exposed. Appl Surf Sci 484:424–432. https://doi.org/10.1016/j.apsusc.2019.04.105

Liu YH, Hsi HC, Li KC, Hou CH (2016) Electrodeposited manganese dioxide/activated carbon composite as a high-performance electrode material for capacitive

deionization. ACS Sustain Chem Eng 4:4762–4770. https://doi.org/10.1021/acssuschemeng.6b00974

Liu H, Liu J, Yang Z, Tang D (2019) Controlled construction of hierarchical hollow micro/nano urchin-like b-MnO_2 with superior lithium storage performance. J Alloys Compd 795:336–342. https://doi.org/10.1016/j.jallcom.2019.04.317

Ma Q, Wang H, Zhang H et al (2017) Fabrication of MnO_2/TiO_2 nano-tube arrays photoelectrode and its enhanced visible light photoelectrocatalytic performance and mechanism. Sep Purif Technol 189:193–203. https://doi.org/10.1016/j.seppur.2017.08.007

Mafa PJ, Mamba BB, Kuvarega AT (2020a) Construction of hierarchical $BiPW_{12}O_{40}$/BiOI p–n heterojunction with enhanced visible light activity for degradation of endocrine disrupting bisphenol A. Sep Purif Technol 253:117349. https://doi.org/10.1016/j.seppur.2020.117349

Mafa PJ, Patala R, Mamba BB et al (2020b) Plasmonic Ag_3PO_4/EG photoanode for visible light-driven photoelectrocatalytic degradation of diuretic drug. Chem Eng J 393:124804. https://doi.org/10.1016/j.cej.2020.124804

Mafa PJ, Swana US, Liu D et al (2021) Synthesis of Bi_5O_7I-MoO_3 photocatalyst via simultaneous calcination of BiOI and MoS_2 for visible light degradation of ibuprofen. Colloids Surfaces A Physicochem Eng Asp 612:126004. https://doi.org/10.1016/j.colsurfa.2020.126004

Mahajan AP, Kondawar SB, Mahore RP, Meshram BH (2015) Polyaniline/MnO_2 nanocomposites based stainless steel electrode modified enzymatic urease biosensor. Procedia Mater Sci 10:699–705. https://doi.org/10.1016/j.mspro.2015.06.075

Malefane ME (2020) Co_3O_4/$Bi_4O_5I_2$/Bi_5O_7I C-scheme heterojunction for degradation of organic pollutants by light-emitting diode irradiation. ACS Omega 5:26829–26844.https://doi.org/10.1021/acsomega.0c03881

Muhambihai P, Rama V, Subramaniam P (2020) Photocatalytic degradation of aniline blue, brilliant green and direct red 80 using NiO/CuO, CuO/ZnO and ZnO/NiO nanocomposites. Environ Nanotechnol Monit Manag 14: 100360. https://doi.org/10.1016/j.enmm.2020.100360

Nikokavoura A, Trapalis C (2018) Graphene and g-C_3N_4 based photocatalysts for NO_x removal: a review. Appl Surf Sci 430:18–52. https://doi.org/10.1016/j.apsusc.2017.08.192

Ntsendwana B, Sampath S, Mamba BB, Arotiba OA (2013) Photoelectrochemical oxidation of p-nitrophenol on an expanded graphite-TiO_2 electrode. Photochem Photobiol Sci 12:1091–1102. https://doi.org/10.1039/c3pp25398h

Orimolade BO, Koiki BA, Peleyeju GM, Arotiba OA (2019) Visible light driven photoelectrocatalysis on a FTO/$BiVO_4$/BiOI anode for water treatment involving emerging pharmaceutical pollutants. Electrochim Acta 307:285–292. https://doi.org/10.1016/j.electacta.2019.03.217

Ouyang K, Xie S, Wang P et al (2019) A novel visible-light responsive photocatalytic fuel cell with a highly efficient $BiVO_4$/WO_3 inverse opal photoanode and a MnO_2/graphene oxide nanocomposite modified cathode. Int J Hydrogen Energy 44:7288–7299. https://doi.org/10.1016/j.ijhydene.2019.01.241

Paula A, Pereira R, Antonio D et al (2019) H_2O_2-assisted photoelectrocatalytic degradation of mitoxantrone using CuO nanostructured films: identification of by-products and toxicity. Sci Total Environ 651:2845–2856. https://doi.org/10.1016/j.scitotenv.2018.10.173

Peleyeju MG, Arotiba OA (2018) Recent trend in visible-light photoelectrocatalytic systems for degradation of organic contaminants in water/wastewater. Environ Sci Water Res Technol 4:1389–1411. https://doi.org/10.1039/c8ew00276b

Pradeep Kumar BM, Sriram Karikkat R, Hari Krishna TH, Udayashankara KSBN (2014) Synthesis, characterization of nano MnO_2 and its adsorption characteristics over an azo dye. Res Rev J Mater Sci 2:27–31

Rouse JD (2015) Development of environmentally sustainable methods for treatment of domestic wastewater and handling of sewage sludge on Yap Island. Sustainability 7:12452–12464. https://doi.org/10.3390/su70912452

Sankar S, Sharma SK, An N et al (2016) Photocatalytic properties of Mn-doped NiO spherical nanoparticles synthesized from sol-gel method. Optik (stuttg) 127:10727–10734. https://doi.org/10.1016/j.ijleo.2016.08.126

Sithole MP, Mafa PJ, de Kock LA, et al (2021) Visible light active g-C_3N_4 sheets/CdS heterojunction photocatalyst for decolourisation of acid blue (AB-25). J Nanoparticle Res 23.https://doi.org/10.1007/s11051-020-05114-z

Su T, Zhao B, Fan B et al (2019) Enhanced microwave absorption properties of novel hierarchical core-shell δ/α MnO_2 composites. J Solid State Chem 273:192–198. https://doi.org/10.1016/j.jssc.2019.01.020

Tang W, Zhang Y, Chen X, Zeng X (2018) Fe_2O_3/TiO_2 film electrodes prepared by the forced hydrolysis method and their photoelectrocatalytic performance. Mater Lett 217:109–112. https://doi.org/10.1016/j.matlet.2018.01.060

Trzci K, Szkoda M, Sawczak M, Karczewski J (2016) Visible light activity of pulsed layer deposited $BiVO_4$/MnO_2 films decorated with gold nanoparticles: the evidence for hydroxyl radicals formation. Appl Surf Sci 385:199–208. https://doi.org/10.1016/j.apsusc.2016.05.115

Umukoro EH, Kumar N, Ngila JC, Arotiba OA (2018) Expanded graphite supported p-n MoS_2-SnO_2 heterojunction nanocomposite electrode for enhanced photoelectrocatalytic degradation of a pharmaceutical pollutant expanded graphite supported p-n MoS_2-SnO_2 heterojunction nanocomposite electrode for enhanced. J Electroanal Chem 827:193–203. https://doi.org/10.1016/j.jelechem.2018.09.027

Wang J, Jiang Y, Ma A et al (2019a) Charge compensation doping to improve the photocatalytic and photoelectrochemical activities of Ta_3N_5: a theoretical study. Appl Catal B Environ 244:502–510. https://doi.org/10.1016/j.apcatb.2018.11.076

Wang Q, Gao Q, Wu H et al (2019b) Separation and purification technology in situ construction of semimetal Bi modified BiOI-Bi_2O_3 film with highly enhanced photoelectrocatalytic performance. Sep Purif Technol 226:232–240. https://doi.org/10.1016/j.seppur.2019.06.002

Wang Q, Ma Y, Liang X et al (2019c) Flexible supercapacitors based on carbon nanotubes-MnO_2 nanocomposite film electrode. Chem Eng J 371:145–153. https://doi.org/10.1016/j.cej.2019.04.021

Wang S, Wang L, Xu X et al (2019d) MnO_2 nanosheet-mediated ratiometric fluorescence biosensor for MicroRNA detection and imaging in living cells. Anal Chim Acta 1063:152–158. https://doi.org/10.1016/j.aca.2019.02.049

Wu P, Liu Z, Chen D et al (2018) Flake-like NiO/WO_3 p-n heterojunction photocathode for photoelectrochemical water splitting. Appl Surf Sci 440:1101–1106. https://doi.org/10.1016/j.apsusc.2018.01.292

Yasmeen H, Zada A, Liu S (2019) Dye loaded MnO_2 and chlorine intercalated g-C_3N_4 coupling impart enhanced visible light photoactivities for pollutants degradation. J Photochem Photobiol A Chem 380:1–9

Zhang Y, Wu M, Kwok YH et al (2019a) In-situ synthesis of heterojunction TiO_2/MnO_2 nanostructure with excellent performance in vacuum ultraviolet photocatalytic oxidation of toluene. Appl Catal B Environ Environ 259:1–11

Zhang Z, Xu Z, Yao Z et al (2019b) Ultrahigh capacitance of TiO_2 nanotube arrays/C/MnO_2 electrode for supercapacitor. J Alloys Compd 805:396–403. https://doi.org/10.1016/j.jallcom.2019.07.070

Zhao B, Lu M, Wang Z et al (2016) Self-assembly of ultrathin MnO_2/graphene with three-dimension hierarchical structure by ultrasonic-assisted co-precipitation method. J Alloys Compd 663:180–186. https://doi.org/10.1016/j.jallcom.2015.12.018

Zhu G, Zhu J, Jiang W et al (2017) Surface oxygen vacancy induced α-MnO_2 nanofiber for highly efficient ozone elimination. Appl Catal B Environ 209:729–737. https://doi.org/10.1016/j.apcatb.2017.02.068